Journal of Fluids and Structures 109 (2022) 103454

Contents lists available at ScienceDirect

Journal of Fluids and Structures

journal homepage: www.elsevier.com/locate/jfs

Flutter stability analysis of an elastically supported flexible foil. Application to the energy harvesting of a fully-passive flexible flapping-foil of small amplitude

R. Fernandez-Feria

Fluid Mechanics, Universidad de Málaga, Dr Ortiz Ramos s/n, 29071 Málaga, Spain

ARTICLE INFO

Article history:
Received 2 September 2021
Received in revised form 27 October 2021
Accepted 19 November 2021
Available online 22 December 2021

Keywords:
Flutter
Oscillating foil
Fluid–structure interaction
Energy harvesting

ABSTRACT

The aerodynamic forces on an oscillating flexible foil are used to study the flutter instability when the flexible foil is elastically mounted to translational and torsional springs and dampers at an arbitrary pivot axis. The present linear theory, valid for small amplitudes of the heaving, pitching and flexural deflection motions, and therefore valid for sufficiently large stiffness ratios, characterizes analytically the onset of the flutter instability and the corresponding leading frequency in terms of the flow velocity and all the structural parameters of the system. The analysis may serve to guide the search for the parametric ranges of energy extraction by a fully-passive flexible flapping-foil hydrokinetic turbine, including the effect of some relevant nondimensional parameters which have not been considered before. The results for the rigid-foil case are validated with recent numerical simulations for a fully-passive flapping-foil turbine. As the stiffness of the foil decreases, the coupled-mode flutter instability of the elastically supported rigid foil may weaken and disappear, or become enhanced, depending on the remaining parameters, most particularly on the location of the centre of mass in relation to the pivot point, whose dependence is investigated for specific values of the rest of the nondimensional parameters.

1. Introduction

Flutter instability of airplane wings, the dynamic instability generating self-sustained oscillations of great violence above a critical speed, is a well studied problem since the early days of flight (Fung, 1969). Actually, one of the earliest and most cited works on unsteady aerodynamic forces on an oscillating airfoil was in fact an analysis of the onset of the flutter instability to mitigate its effect in aeronautics (Theodorsen, 1935).

Interest in coupled-mode (pitch–plunge) flutter instability has been recently renewed because of its relevance in the field of energy harvesting through hydrokinetic turbines based on fluid–structure instabilities of an elastically supported foil immersed in a fluid current (Peng and Zhu, 2009; Zhu, 2012; Boragno et al., 2012; Veilleux and Dumas, 2017; Wang et al., 2017; Boudreau et al., 2018; Duarte et al., 2019). Despite their more intricate mechanism, most of the studies of flapping-foil turbines have focused on investigating the energy harvesting performance of rigid flapping-foil turbines with fully prescribed kinematics or with semipassive systems because of their alleged better efficiencies (Kinsey and Dumas, 2008; Shimizu et al., 2008; Zhu et al., 2009; Zhu and Peng, 2009; Abiru and Yoshitake, 2011; Xiao and Zhu, 2014; Young et al., 2014; Su and Breuer, 2019; Boudreau et al., 2019b,a; Ma et al., 2021). But recent studies have shown

E-mail address: ramon.fernandez@uma.es.

https://doi.org/10.1016/j.jfluidstructs.2021.103454

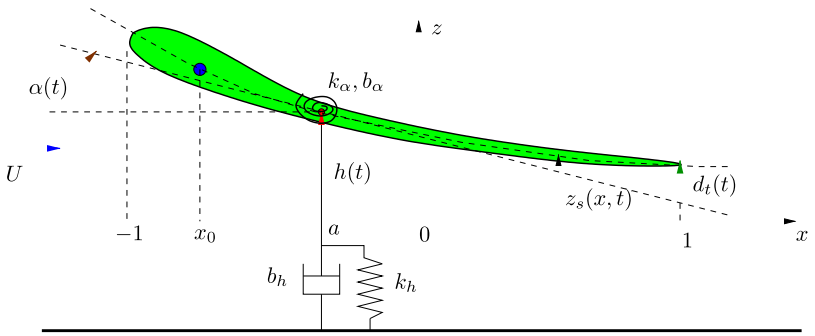

Fig. 1. Schematic of the fully-passive flexible flapping-foil (all quantities are dimensionless, except the velocity U). The blue dot ($x = x_0$) is the centre of mass and the red one ($x = a$) the pitch axis. (For interpretation of the references to colour in this figure legend, the reader is referred to the web version of this article.)

that the mechanically simpler fully-passive concept, with both rigid-foil degrees of freedom elastically supported, and therefore triggered by flutter instabilities, may achieve comparable, or even larger, efficiencies than most fully-constrained or semipassive systems (Boudreau et al., 2020).

Although the study of the large-amplitude motions that can result from the coupled-mode flutter instability, as well as the stall flutter and other non-linear aeroelastic instabilities, are of utmost importance for analysing the performance of these fully-passive flapping-foil turbines (Dowell, 2015; Amandolese et al., 2013; Poirel and Mendes, 2014; Pigolotti et al., 2017; Boudreau et al., 2019b,a; Zhu et al., 2020), the determination of the instability onset from small perturbations is also very relevant in the field, because it easily provides a good estimation of the full parametric ranges for energy harvesting without the use of costly numerical simulations or experiments, which necessarily have to be made within very limited parametric ranges.

For pitch–plunge oscillations of a rigid foil the determination of the flutter instability has been widely studied because of its importance in aeronautics and because, as a consequence of this relevance, simple analytical expressions for the force and moment on small-amplitude pitching and plunging airfoils were derived in the early days of flight (Theodorsen, 1935; Sears, 1941; Fung, 1969; Bisplinghoff and Ashley, 1975). For a flexible foil undergoing flexural deflection, also of small amplitude, simple analytical expressions for the force, pitching moment and *flexural* moment about an arbitrary pivot axis were very recently derived (Alaminos-Quesada and Fernandez-Feria, 2020) using a linearized vortex impulse theory (von Kármán and Sears, 1938; Fernandez-Feria, 2016). These expressions are employed in the present work in combination with the linearized fluid–structure interaction through the first three moments of the Euler–Bernoulli beam equation for a quartic polynomial deflection (Fernandez-Feria and Alaminos-Quesada, 2021a,b) to derive analytical expressions for the onset of the "pitch–plunge–flexural" oscillations arising from the flutter instability of an elastically supported flexible foil. Then, some results, both for rigid and flexible foils, are presented and discussed in relation to the energy harvesting problem by a fully-passive flexible flapping-foil turbine. Some of the present theoretical results for rigid foils are compared satisfactorily with recent results obtained from numerical simulations (Boudreau et al., 2020). Semi-actuated flexible flapping-foil turbines have also been considered, but with prescribed wing deformation and therefore without considering the fluid–structure interaction (Liu et al., 2013), so that a direct comparison in terms of the structural parameters of the elastically supported system is not possible.

The related problem of flutter instability of *clamped* flexible plates in a two-dimensional flow has also been thoroughly analysed by solving numerically the resulting nonlinear eigenvalue problem, uncovering a broad and intricate spectrum of unstable modes as the stiffness of the foil decreases (e.g., Guo and Païdoussis, 2000; Tang and Païdoussis, 2007; Alben, 2008; Floryan and Rowley, 2018), including its application to energy harvesting (Tang et al., 2009). Though these results are not for the elastically supported foils considered here, some of them are used to characterize the stiffness range of validity of the present analytical results.

2. Formulation of the problem

A flexible foil of chord length c immersed in a uniform current with velocity U along the x-axis of an inviscid and incompressible fluid with density ρ is considered. Except otherwise specified, all the parameters and variables used from this point onwards are dimensionless, scaled with the flow speed U, the half-chord length $c/2$ and the density ρ. Thus, for instance, the foil at rest is located along the x-axis between $x = -1$ and $x = 1$ and time is scaled with $c/(2U)$. Due to the fluid–structure interaction (FSI), the foil may be displaced along the z-axis with a motion characterized by the position of its centreline $z_s(x, t)$, which is obtained here assuming small amplitude, i.e., $|z_s| \ll 1$, so that it always lies in $-1 \le x \le 1$, approximately (see Fig. 1).

The foil is attached to translational and torsional springs and dampers at the pitch axis, located at $x = a$, which does not necessarily coincide with its centre of mass $x = x_0$. Thus, at this point $x = a$, the foil just undergoes a passive (and,

therefore, unknown) heaving and pitching motion characterized by the translational and angular displacements $h(t)$ and $\alpha(t)$, respectively; i.e.,

$$z_s(a,t) = h(t), \quad \left.\frac{\partial z_s}{\partial x}\right|_{x=a} = -\alpha(t). \tag{1}$$

If the chordwise flexural deformation of the foil is also small, z_s may be approximated by a quartic polynomial (Fernandez-Feria and Alaminos-Quesada, 2021a)

$$z_s(x,t) = h(t) - (x-a)\alpha(t) + (x-a)^2 d(t) - (x-a)^3 \frac{2d(t)}{3(1-a)} + (x-a)^4 \frac{d(t)}{6(1-a)^2}\,, \tag{2}$$

which, in addition to (1), satisfies the boundary conditions $\partial^2 z_s/\partial x^2 = \partial^3 z_s/\partial x^3 = 0$ at $x = 1$, corresponding to a free trailing edge. The function $d(t)$ characterizes the chordwise flexural deflection. In particular, the flexural deflection at the trailing edge relative to an identical rigid foil with the same heaving and pitching motion is $d_t(t) = (1-a)^2 d(t)/2$.

If k_h and k_α are the (dimensionless) stiffnesses of the translational and torsional springs, respectively, and b_h and b_α the respective constants of the translational and torsional dampers used to extract energy from the current, the nondimensional output force and torque (per unit chord-length) that the foil exerts at $x = a$ can be written as

$$C_{L_o} = \frac{L_o}{\frac{1}{2}\rho U^2 c} = k_h h + b_h \dot{h}\,, \tag{3}$$

$$C_{Mo} = \frac{M_o}{\frac{1}{2}\rho U^2 c^2} = -k_\alpha \alpha - b_\alpha \dot{\alpha}\,, \tag{4}$$

where a dot denotes differentiation with respect to time. Note that the moment is defined positive when counterclockwise, while α increases clockwise to follow the usual convention in aerodynamics (see Fig. 1).

If one substitutes the foil deflection (2) into the Euler–Bernoulli beam equation that includes (3) and (4) as punctual force and torque, respectively, at $x = a$, the first three moments of that equation, i.e., that equation integrated along the chord-length as well as the integration of that equation previously multiplied by $x - a$ and by $(x-a)^2$, can be written as (Fernandez-Feria and Alaminos-Quesada, 2021a,b)

$$m\left[\ddot{h} + (a - x_0)\ddot{\alpha}\right] + J_a \ddot{d} + \frac{16}{3(1-a)^2} S\, d = C_L - k_h h - b_h \dot{h}\,, \tag{5}$$

$$m(x_0 - a)\ddot{h} - I_a \ddot{\alpha} + J_d \ddot{d} - \frac{16a}{3(1-a)^2} S\, d = 2\left(C_M + k_\alpha \alpha + b_\alpha \dot{\alpha}\right)\,, \tag{6}$$

$$I_a \ddot{h} - I_a \ddot{\alpha} + K_d \ddot{d} + \frac{16}{3}\frac{a^2 + \frac{1}{3}}{(1-a)^2} S\, d = C_F\,. \tag{7}$$

In these equations, C_L, C_M and C_F are the lift, moment and flexural coefficients, respectively, related to the pressure that the fluid exerts on the foil as

$$C_L(t) = \int_{-1}^{1} \Delta C_p(x,t)dx\,, \quad C_M(t) = \frac{1}{2}\int_{-1}^{1} (x-a)\Delta C_p(x,t)dx\,, \quad C_F = \int_{-1}^{1} (x-a)^2 \Delta C_p(x,t)dx\,, \tag{8}$$

where $\Delta C_p(x,t) = (p^- - p^+)/(\rho U^2)$ is the nondimensional pressure difference between the lower (superscript $^-$) and upper (superscript $^+$) sides of the foil. The nondimensional stiffness of the foil S and its mass ratio R are defined as

$$S(x) = \frac{E(x)\varepsilon^3(x)}{\rho U^2 c^3}\,, \quad R(x) = \frac{\rho_s(x)\varepsilon(x)}{\rho c}\,, \tag{9}$$

where E its elastic modulus of the foil, ρ_s its density, and ε its thickness. These quantities may vary along the chord, but S has been assumed constant in deriving Eqs. (5)–(7). However, the mass ratio R may change with x in the remaining coefficients appearing in (5)–(7) to allow for different values of the centre of mass, moment of inertia and the rest of coefficients, which are defined in terms of $R(x)$ as

$$m = 2\int_{-1}^{1} R dx\,, \quad m(x_0 - a) = 2\int_{-1}^{1} (x-a)R dx\,, \qquad x_0 = \frac{2}{m}\int_{-1}^{1} xR dx\,, \tag{10}$$

$$I_a = 2\int_{-1}^{1} (x-a)^2 R dx\,, \tag{11}$$

$$J_a = 2\int_{-1}^{1}\left[(x-a)^2 - \frac{2}{3}\frac{(x-a)^3}{1-a} + \frac{(x-a)^4}{6(1-a)^2}\right]R dx\,, \tag{12}$$

$$I_d = 2\int_{-1}^{1}(x-a)^3 R dx\,, \tag{13}$$

$$J_d = 2\int_{-1}^{1}\left[(x-a)^3 - \frac{2}{3}\frac{(x-a)^4}{1-a} + \frac{(x-a)^5}{6(1-a)^2}\right]R dx\,, \tag{14}$$

$$K_d = 2\int_{-1}^{1}\left[(x-a)^4 - \frac{2}{3}\frac{(x-a)^5}{1-a} + \frac{(x-a)^6}{6(1-a)^2}\right]R dx\,. \tag{15}$$

For a rigid foil ($d = 0$), only three of these parameters remain: the nondimensional mass of the foil m, the nondimensional static moment $m(x_0 - a)$, where x_0 is the foil's centre of mass, and the nondimensional moment of inertia about the pitch axis I_a. The rest of parameters are associated to the flexural deflection $d(t)$, characterizing its mechanical coupling with the heaving and pitching motions in the present approach. Thus, J_a relates the flexural acceleration to the vertical force, J_d to the pitching moment and K_d to the flexural moment, while I_d relates the pitching acceleration to the flexural moment. In Appendix A are listed the values of all these parameters in two relevant situations: for a constant mass ratio R, in which case, for instance, the centre of mass lies at the centre of the foil ($x_0 = 0$) and $I_a = 4R(a^2 + 1/3)$, and for a distribution $R(x)$ such that m, x_0 and I_a can be selected arbitrarily and independent of each other.

In the limit of a rigid foil ($S \to \infty$), the flexural Eq. (7) correctly yields the vanishing deflection as $|d| \sim S^{-1}$. However, this means that the terms containing S in Eqs. (5) and (6) do not vanish in this limit, so that the rigid-foil equations for the vertical force and for the moment about the pivot axis are not correctly recovered. But this is an artefact of the present approximation, where the displacement (2) is truncated as a quartic polynomial. This situation can be fixed by using higher polynomial approximations for z_s and selecting the new coefficients so that these two terms vanish, while retaining the corresponding term in (7). However, this would complicate unnecessarily the present approximation which minimally accounts for the stiffness effect within the Euler–Bernoulli beam equation, because the resulting expressions for C_L, C_M, C_F would become cumbersome. Thus, the simplest approach with Eqs. (5) and (6) without the S-terms, and Eq. (7) with that term from the present quartic approximation, is adopted here as a lowest order, or minimal, model that takes into account the flexibility of the foil, valid for sufficiently large stiffness S and for frequencies below the second natural frequency of the system. As shown below, this approach reproduces accurately the frequency of the *first* unstable mode for sufficiently large stiffness (Alben, 2008), and previous numerical results for the energy harvesting of a fully-passive flapping-foil turbine (Boudreau et al., 2020). These comparisons will thus constitute a validation of the present lowest order formulation.

3. Flutter instability

Once the force and moment coefficients (8) are written in terms of the foil deflection (2), Eqs. (5)–(7) constitute a system of three linear differential equations for $h(t)$, $\alpha(t)$ and $d(t)$ for given initial conditions. Of particular interest for energy harvesting devices is the study of the flutter instability, through which any small disturbance of the airfoil can serve as a trigger to initiate an oscillation of great violence (Fung, 1969). Thus, to analyse the onset of this instability, and therefore the parametric range in which energy is transferred from the flow to the structure so that the foil may work as an energy harvester, as well as obtain the frequency ω of the subsequent oscillations, we consider solutions of the form

$$h(t) = \mathrm{Re}\left[H_0 e^{i\gamma t}\right], \quad \alpha(t) = \mathrm{Re}\left[A_0 e^{i\gamma t}\right], \quad d(t) = \mathrm{Re}\left[D_0 e^{i\gamma t}\right], \tag{16}$$

where Re means real part and γ, H_0, A_0 and D_0 are in general complex quantities, with

$$\gamma = k + i\sigma\,, \quad k = \frac{\omega c}{2U}\,, \tag{17}$$

being k the nondimensional (or reduced) frequency and $-\sigma$ the nondimensional growth rate. The absolute values of H_0, A_0 and D_0 are the amplitudes of the heaving, pitching and flexural components of the foil motion, respectively, while their angles correspond to their relative phase shifts. For this harmonic motion the coefficients (8) can be expressed in a closed analytical form (see Appendix B), so that Eqs. (5)–(7) are transformed into a linear system of three algebraic, complex equations for H_0, A_0 and D_0:

$$\mathbf{A}(\gamma)\cdot\mathbf{X} = \mathbf{0} \quad \text{with} \quad \mathbf{A} = \begin{pmatrix} A_{11} & A_{12} & A_{13} \\ A_{21} & A_{22} & A_{23} \\ A_{31} & A_{32} & A_{33} \end{pmatrix}, \quad \mathbf{X} = \begin{pmatrix} H_0 \\ A_0 \\ D_0 \end{pmatrix}, \tag{18}$$

where the different coefficients A_{ij} are given in Appendix C.

For a given set of values of the different nondimensional parameters, the system has nontrivial solutions for specific (eigen-)values of γ satisfying

$$\det[\mathbf{A}(\gamma)] = 0\,, \tag{19}$$

fixing the frequency of the subsequent oscillations of the system k if it is unstable, i.e., if $\sigma < 0$. On the contrary, if $\sigma > 0$, any small perturbation in z_s will be damped. Thus, of particular relevance for the energy harvesting problem is the characterization of the neutral hyper-surface in the parameter space at which $\sigma = 0$ and the corresponding *natural* frequencies, $k = k_n$ say. Within the region of the parameter space where $\sigma < 0$, a passive motion of the foil is allowed according to the present linear theory, which may be used to extract energy from the current. This region and the corresponding frequencies will be explored below for several particular cases. However, the present linear (stability) theory does not provide the final amplitudes of the ensuing oscillating motion of the flexible foil. Therefore, one *cannot obtain* from the present analysis the output power nor the efficiency of the resulting fully-passive energy harvesting system.

Eq. (19) for the complex eigenvalue γ is solved numerically using the Matlab function *fsolve*, starting from the leading neutral frequency corresponding to a rigid foil when the FSI is neglected, whose analytical expression is given in the next section. As explained below, this neutral frequency is the *first* resonant frequency of the rigid-foil system in vacuo, so that only the leading eigenvalue associated to this first natural mode as $S \to \infty$ is considered here. This is consistent with the present approximation valid for small deflection and, consequently, for sufficiently large stiffnesses, capturing only the lowest frequency mode. To check the validity of the present results for a flexible foil, they are compared in Section 5.1 below with previous ones obtained numerically by Alben (2008) for a flexible foil clamped at the leading edge. Therefore, the comparison is made by setting very large stiffnesses of the linear and torsional springs in the present configuration. As we shall see, the present results recover the leading eigenvalue for $S \gtrsim 1$, but higher instability modes appearing as S decreases below unity are not correctly recovered from the present approximation.

4. Rigid foil

Considering first the case of a rigid foil ($S \to \infty$), so that the flexural deflection amplitude vanishes, $D_0 = 0$, a nontrivial solution exists if $\det(\mathbf{A}_0) = 0$, with

$$\mathbf{A}_0 = \begin{pmatrix} A_{11} & A_{12} \\ A_{21} & A_{22} \end{pmatrix}. \tag{20}$$

If one neglects the FSI (i.e., neglecting the contributions A_{ij}^F to the coefficients given in Appendix C), the expressions for the different A_{ij} are particularly simple. If, in addition, $k_h \to \infty$, so that there is no heaving motion ($H_0 = 0$), a nontrivial pitching solutions exists if $A_{22} = 0$, yielding

$$\gamma = \frac{2ib_\alpha \pm \sqrt{8I_a k_\alpha - 4b_\alpha^2}}{2I_a}\,, \tag{21}$$

so that $\sigma \geq 0$ and the system is always stable. The neutral stability case ($\sigma = 0$, $\gamma = k = k_n$) occurs for $b_\alpha = 0$ with the natural frequency (only the positive frequency is written)

$$k_n = k_{r\alpha} = \sqrt{\frac{2k_\alpha}{I_a}}\,, \tag{22}$$

which is the nondimensional first resonant frequency of a plate attached to a torsional spring in vacuum. (Note that for $b_\alpha > \sqrt{2I_\alpha k_\alpha}$, one gets $k = 0$ and $\sigma > 0$, so that all perturbations are straightforwardly damped.)

Alternatively, if $k_\alpha \to \infty$, so that the pitching motion is inhibited ($A_0 = 0$), heaving motion may exist if $A_{11} = 0$; i.e., if

$$\gamma = \frac{ib_h \pm \sqrt{4\,mk_h - b_h^2}}{2m}\,. \tag{23}$$

Again, the system is always stable ($\sigma \geq 0$), with the neutrally stable case for $b_h = 0$, corresponding to the natural frequency

$$k_n = k_{rh} = \sqrt{\frac{k_h}{m}}\,, \tag{24}$$

which is the nondimensional first resonant frequency of a plate attached to a linear spring in vacuum. Again, for $b_h > 2\sqrt{mk_h}$, the system is strongly damped ($\sigma > 0$, $k = 0$).

In general, when the FSI is neglected, $\det(\mathbf{A}_0) = 0$ can be written as

$$(-m\gamma^2 + k_h + b_h i\gamma)(I_a\gamma^2 - 2k_\alpha - 2b_\alpha i\gamma) + m^2\gamma^4(a - x_0)^2 = 0\,. \tag{25}$$

Table 1
Equivalence between the present nondimensional parameters for a rigid foil and those used in Boudreau et al. (2020).

Present	k	m	$m(x_0-a)$	k_h	b_h	I_a	k_α	b_α	$k_{r\alpha}$	k_{rh}
Boudreau et al. (2020)	πf^*	$4m_h^*$	$8S^*$	k_h^*	$2D_h^*$	$16I_\theta^*$	$2k_\theta^*$	$4D_\theta^*$	$\pi f_{n,\theta}^*$	$\pi f_{n,h}^*$

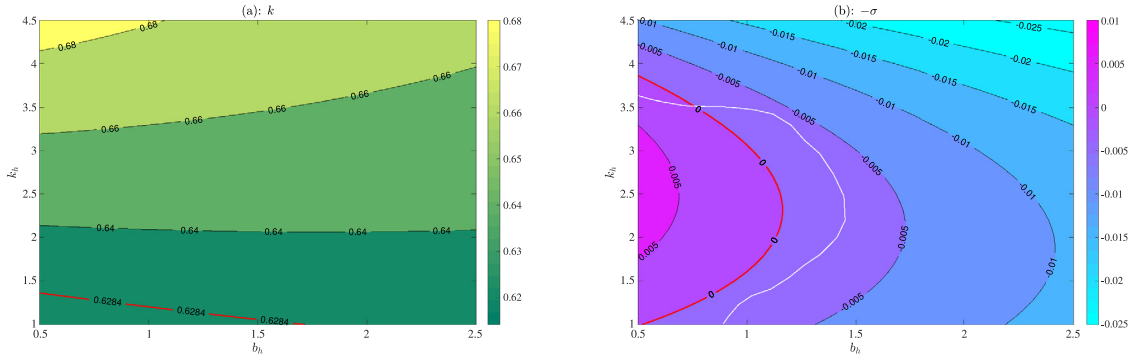

Fig. 2. Contours of k (a) and $-\sigma$ (b) in the $b_h - k_h$ plane for $b_\alpha = 0$, $m = 8$, $a = -1/2$, $x_0 = -0.1$, $I_a = 32$, $k_\alpha = 6.32$. Red thick lines correspond to $k = k_{r\alpha}$ in (a) and to $\sigma = 0$ in (b). The white line in (b) is the contour for 10% of the maximum power coefficient in figure 2(e) of Boudreau et al. (2020). (For interpretation of the references to colour in this figure legend, the reader is referred to the web version of this article.)

For neutral stability, the imaginary part of this expression vanishes if

$$k_n = k_{n0} = \sqrt{\frac{2(b_\alpha k_h + b_h k_\alpha)}{2\, m b_\alpha + I_\alpha b_h}}\,. \tag{26}$$

Note that this frequency coincides with $k_{r\alpha}$ when $b_\alpha = 0$ and with k_{rh} if $b_h = 0$, but we shall not consider this last situation in what follows (only the cases in which the energy is totally, or mainly, harvested by the heave damper will be considered). It turns out that, again, $\sigma \geq 0$, so that the system is stable, no flutter instability exists and no energy can be harvested, which was to be expected since the FSI has been neglected.

4.1. Comparison with recent numerical results

To analyse the effect of the fluid–structure interaction on a rigid foil, we consider first one of the two set of cases studied by Boudreau et al. (2020), who integrated numerically the full Navier–Stokes equations for this problem. Thus, in addition to $b_\alpha = 0$, we select $m = 8$, $x_0 = -0.1$, $I_a = 32$, $a = -1/2$, $k_\alpha = 6.32$, and varying b_h and k_h (using the equivalence between the respective parameters summarized in Table 1, the corresponding values of these authors' parameters are $D_\theta^* = 0$, $m_h^* = 2$, $S^* = 0.4$, $I_\theta^* = 2$, pitch axis at the quarter-chord point, $k_\theta^* = 3.16$, $0.25 \leq D_h^* \leq 1.25$ and $1 \leq k_h^* \leq 4.5$, respectively). Fig. 2 shows the values of k and σ corresponding to $\det(\mathbf{A}) = 0$ in the $b_h - k_h$ plane. It is observed that the system is unstable within an almost "parabolic" region of that plane for $b_h \lesssim 1.16$. Additionally, the frequency k [Fig. 2(a)] remains always very close to the resonant frequency $k_{r\alpha}$ given by (22), also marked in that figure ($k_{r\alpha} \simeq 0.6284$ in the present case). Both these results are in agreement with Boudreau et al. (2020): the frequency is not shown in their Fig. 2 because it remains very close to the resonant frequency, and the "parabolic" region with $\sigma \leq 0$ in Fig. 2(b) is quite similar to that in their Fig. 2(e) for which there is a significant power output. Fig. 2(b) also shows with a white line the contour corresponding to 10% of the maximum power coefficient obtained numerically by these authors, thus enclosing the region with significant power output due to the flutter instability. The irregularity of this contour line is due to the finite number of pairs of values (b_h, k_h) for which numerical simulations are performed.

Incidentally, if the instability region in Fig. 2(b) is written as $b_h \leq b_h^*(k_h; a, x_0, I_a, \ldots)$, where b_h^* is the function of k_h for given a, x_0, I_a, etc., corresponding to the neutral curve with $\sigma = 0$ in Fig. 2(a), the so-called *flutter velocity* U^* for the present set of parameters can be obtained by just writing the above condition in terms of dimensional magnitudes (marked with a " ˜ " whenever the symbol is the same):

$$b_h = \frac{2\tilde{b}_h}{\rho U c} \leq b_h^*\,, \quad U \geq U^* = \frac{\tilde{b}_h}{\rho c\; b_h^*(k_h; a, x_0, I_a, \ldots)}\,. \tag{27}$$

The minimum flutter velocity corresponds to the maximum value of b_h^*, which for the present case is approximately 1.16.

To further corroborate this agreement, we also consider here results by Boudreau et al. (2020) when the spring constant k_h and the mass ratio m are simultaneously varied, but maintaining constant the nondimensional static moment S^* (see Table 1 for the relation between S^* and m, x_0 and a). These authors found that the narrow range of values of k_h

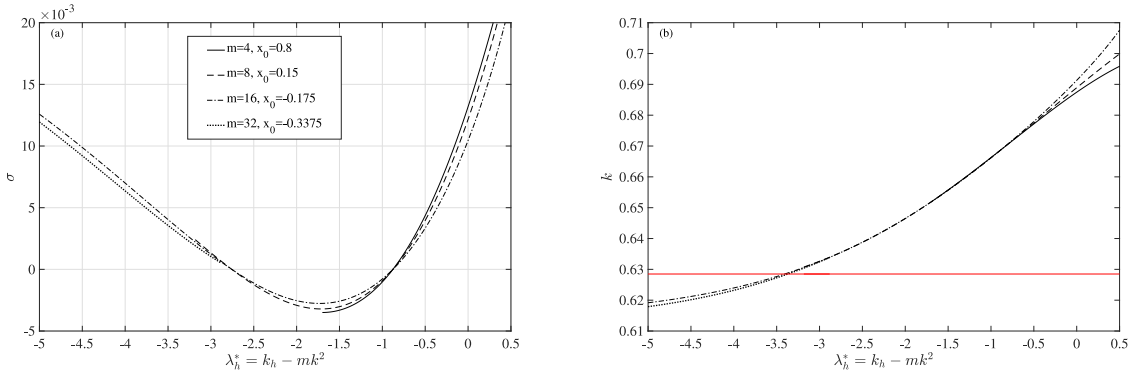

Fig. 3. σ (a) and k (b) vs. λ_h^* given by Eq. (28) when k_h is varied from zero onwards for different values of m and x_0, as indicated (see main text). $a = -1/2$, $b_h = 1.5$, $mx_0 = 4.7$, $I_a = 32$, $b_\alpha = 0$, $k_\alpha = 6.32$. The red line in (b) is $k_{r\alpha}$. (For interpretation of the references to colour in this figure legend, the reader is referred to the web version of this article.)

where energy harvesting is possible, which depends strongly on m (see their Fig. 6), collapse into a common range when represented in terms of the parameter they called the effective heave stiffness λ_h^* (see their figure 7(e)), which in the present notation can be written as

$$\lambda_h^* = k_h - mk^2 = m(k_{rh}^2 - k^2)\,. \tag{28}$$

Boudreau et al. (2020) found that the energy harvesting range is roughly between -3 and -1, with the best performance about $\lambda_h^* \approx 2$, when $D_h^* = 0.75$, $S^* = 0.65$, $I_\theta^* = 2$, $D_\theta^* = 0$ and $k_\theta =^* 3.16$ (i.e., $b_h = 1.5$, $mx_0 = 4.7$, $I_a = 32$, $b_\alpha = 0$ and $k_\alpha = 6.32$ according to Table 1). Fig. 3(a) plots σ vs. λ_h^* when $k_h \geq 0$ for four values of m (and x_0) corresponding to the four values of m_h^* used by Boudreau et al. (2020) in their §3.2 with constant S^*: namely, $m = 4$ (and $x_0 = 0.8$), $m = 8$ ($x_0 = 0.15$), $m = 16$ ($x_0 = -0.175$), and $m = 32$ ($x_0 = -0.3375$) in the present notation. It is observed that, according to the present linear theory, the flapping-foil works as an energy harvester in roughly the same range of $-3 \lesssim \lambda_h^* \lesssim -1$ predicted by Boudreau et al. (2020), where the fluid-foil system is unstable ($\sigma < 0$), and that in this region all the curves collapse when different values of m and x_0 are used. The maximum growth rate is also found at $\lambda_h^* \approx 2$. For these values of λ_h^* between -3 and -1 the corresponding frequencies plotted in Fig. 3(b) also collapse for the different cases. One may thus conclude that according to the present theory λ_h^* is indeed an excellent unifying parameter to predict the narrow range of values of the different dimensionless parameters for which the rigid-foil can be used as a fully-passive energy harvester, which will operate at about the pitching resonant frequency $k \approx k_{r\alpha}$ [also shown in Fig. 3(b)]. Incidentally, that the operating and optimal values of λ_h^* are negative implies, according to the second equality in (28), that the operating frequency is always larger than the heave resonant frequency in vacuum k_{rh}, as noted by Boudreau et al. (2020).

4.2. Effect of pivot point and spring stiffness

To reduce the number of varying parameters we consider only airfoils with constant mass ratio R, i.e., $x_0 = 0$ and $I_a = m(a^2 + 1/3)$ (see Appendix A), and explore the instability region in the $b_h - k_h$ plane for several values of the torsional spring stiffness k_α and the pivot point location a. For given $m = 4R$ and a we find that no instability exists for k_α larger than a maximum value that for $m = 8$ is about 1.75. Fig. 4 shows the contours of the growth rate $-\sigma$ in the $b_h - k_h$ plane for the pivot point at the quarter-chord length ($a = -1/2$) and two values of k_α, 0.5 and 1. As k_α increases, the region of flutter instability is displaced towards smaller values of the linear damper constant b_h, until it disappears for $k_\alpha \approx 1.75$ for these values of m and a. On the contrary, as k_α decreases, the range of values of k_h for which the system is unstable decreases, becoming $0 \leq k_h \lesssim 2$ for $k_\alpha = 0.25$ (not shown). Thus, there exists an optimal value of k_α, which for the present values of a and m is roughly 0.5, plotted in Fig. 4(a).

To see the effect of the pivot point location, Fig. 5 shows the instability regions for this last mentioned case with $k_\alpha = 0.5$, but with $a = -3/4$ and $a = -1/4$; i.e., pivoting closer to the leading edge and closer to the mid-chord, respectively, than the case plotted in Fig. 4(a). As the pivot point approaches the leading edge, the region of instability is reduced to smaller values of b_h and, specially, smaller values of k_h. Thus, for the case $a = -3/4$ plotted in Fig. 5(a) this region is reduced to $k_h \lesssim 1.25$, and practically disappears when pivoting at the leading edge ($a = -1$, not shown). On the other hand, as the pivot approaches the mid-chord point, the flutter instability region increases towards larger values of b_h, but for diminishing values of k_h, practically disappearing when pivoting at the mid-chord ($a = 0$, not shown). Fig. 5(b) shows the case with $a = -1/4$, with an instability region somewhat larger than for $a = -1/2$, but with smaller growth rates.

Overall, one may conclude that for a rigid and uniform foil with $m = 8$ ($R = 2$) the best performance in terms of a wider flutter instability region and higher growth rates is, according to the present linear theory, for a foil pivoting about

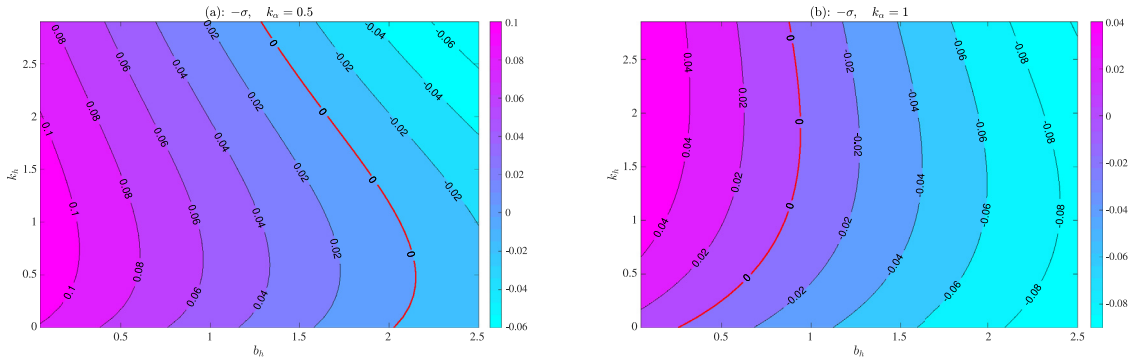

Fig. 4. Contours of the growth rate $(-\sigma)$ in the $b_h - k_h$ plane for a constant mass ratio rigid foil with $k_\alpha = 0.5$ (a) and $k_\alpha = 1$ (b). $b_\alpha = 0$, $m = 8$, $a = -1/2$. The marginal stability curves are highlighted with a thick red line. (For interpretation of the references to colour in this figure legend, the reader is referred to the web version of this article.)

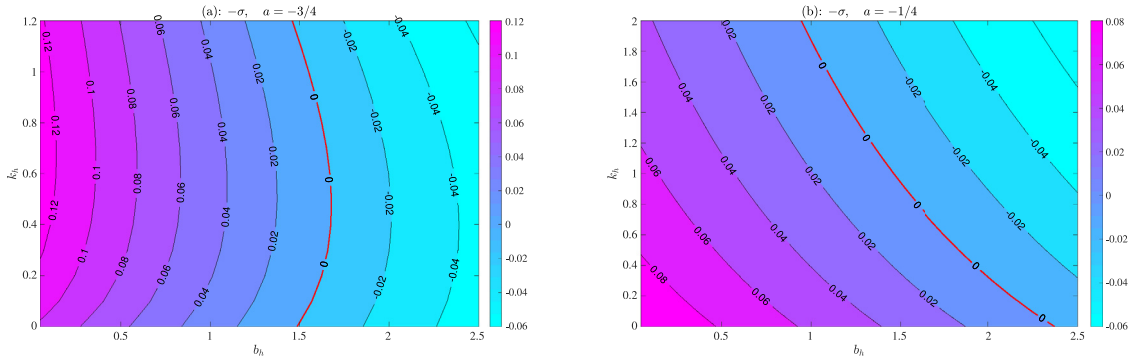

Fig. 5. Contours of $-\sigma$ in the $b_h - k_h$ plane for a constant mass ratio rigid foil pivoting at $a = -3/4$ (a) and at $a = -1/4$ (b). $b_\alpha = 0$, $m = 8$, $k_\alpha = 0.5$. The marginal stability curves are highlighted with a thick red line. (For interpretation of the references to colour in this figure legend, the reader is referred to the web version of this article.)

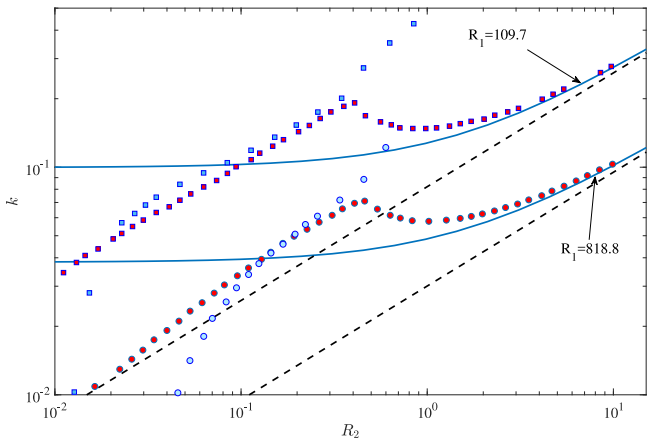

Fig. 6. $k = \mathrm{Re}(\gamma)$ given by (29) vs. $R_2 = 2S/3$ (continuous lines) for two values of $R_1 = 2R$, as indicated, to compare with numerical results from figures (4d) and (4f) in Alben (2008) (symbols; squares for $R_1 = 109.7$ and circles for $R_1 = 818.8$; only the two first modes are plotted, with red symbols for the leading eigenvalues and blue for the following one). The dashed lines correspond to the limit $R_2 \to \infty$ given by (31). (For interpretation of the references to colour in this figure legend, the reader is referred to the web version of this article.)

its quarter-chord, with spring stiffness k_h between 0.5 and 1, and a damper constant b_h smaller than about 2, the smaller the larger the growth rate. The corresponding frequency is always very close to the resonant frequency $k_{r\alpha}$. As the mass ratio decreases, the system becomes more stable, with the instability region displacing towards smaller values of b_h until disappearing. Thus, the most unstable case just mentioned for $m = 8$ becomes stable in all the $b_h - k_h$ plane for $m \lesssim 4$.

Finally, it is worth mentioning that if $k_h \to \infty$ or $k_\alpha \to \infty$ no flutter instability is found, so that *coupled* pitch–plunge motion is always generated when the elastically supported rigid foil becomes unstable according to linear theory (Dowell, 2015).

5. Effect of flexibility

5.1. Clamped foil. Comparison with previous results

Before analysing the effect of flexibility on the unstable modes described in the previous section for a rigid foil, it is of interest to check the validity of the present approximation as rigidity is reduced. To that end we depart in this section from the elastically supported foil at $x = a$, of interest in energy harvesting devices, and consider a clamped foil for which previous results are available for the nonlinear eigenvalue problem. In particular, we consider a clamped foil at the leading edge ($a = -1$), analysed by Alben (2008) within the present inviscid and linear framework, but considering a full expansion of the deflection z_s in Chebyshev polynomials instead of the present quartic polynomial approximation (2). Thus, this author can obtain numerically all the wave number modes, not just the lowest frequency captured by the present minimal approximation, as shown below.

A clamped foil at $x = a$ can be simulated in the present formulation by assuming very large spring stiffnesses, i.e., $k_h \to \infty$ and $k_\alpha \to \infty$. Thus, the pitching and heaving motions are inhibited ($A_0 = H_0 = 0$), and a flexural deflection motion may exist if $A_{33} = 0$, yielding the following eigenvalue equation for γ:

$$-K_d(a)\,\gamma^2 + \frac{16}{3}\frac{a^2+\dfrac{1}{3}}{(1-a)^2}\,S + A_{33}^F(\gamma) = 0\,. \tag{29}$$

Neglecting the FSI (i.e., neglecting the contribution from A_{33}^F) one obtains the neutrally stable mode

$$\gamma = k_{rd} = \pm\frac{4}{3}\sqrt{\frac{(1+3a^2)S}{(1-a)^2K_d(a)}}\,. \tag{30}$$

For a foil with constant R and for $a = -1$, this frequency can be written as (only positive values are considered)

$$k_{rd} \simeq 0.4965\sqrt{\frac{S}{R}} \simeq 0.860\sqrt{\frac{R_2}{R_1}}\,, \tag{31}$$

very close to the leading eigenvalue obtained numerically by Alben (2008), $0.8790\sqrt{R_2/R_1}$, where Alben's nondimensional parameters R_1 and R_2 are related to R and S by $R_1 = 2R$ and $R_2 = 2S/3$, respectively. Thus, as expected for an approximation valid for sufficiently large stiffnesses S, the present model captures only the first, lowest frequency mode, but not the higher ones. This is further corroborated as the rigidity of the foil is decreased in Fig. 6, which plots the real part of this first eigenvalue when the FSI term A_{33}^F is taken into account. It is obtained by solving Eq. (29) starting from (31) for given values of R as S is decreased. In the figure, k is plotted vs. R_2 for $R_1 = 109.7$ and 818.8 to compare with the numerical results for the real part of the different eigenvalues given in figures (4d) and (4f) of Alben (2008), which are represented with symbols in Fig. 6. It is observed that the present k practically coincides with the lowest frequency in figures (4d) and (4f) in Alben (2008) for decreasing R_2 up to $R_2 \approx 1$, below which the other higher modes show up. Therefore the present approximation for large S is valid even for $S \approx 1$. Below this value higher modes with more complex deflections arise, which are not covered by the present theory. The grow rate $\sigma = -\Im(\gamma)$ is not plotted because it is too small for this range of S and these values of R, so that they cannot be distinguished in figures (4c) and (4e) in Alben (2008) to compare with.

5.2. Effect of decreasing rigidity on the unstable rigid modes described in Section 4

The effect of flexibility on the rigid-foil unstable modes described in the preceding section for a foil with uniform mass ratio [Figs. 4 and 5] turns out to be practically negligible when the stiffness S is larger than about 10. This can be neatly observed in Fig. 7, where the frequency and the growth rate are plotted in the $b_h - S$ plane for the case with $k_h = 0.5$ considered in Fig. 4(a). Remember that this was roughly the case with the largest instability region in the parameter space. As S decreases further below 10, the critical value of the damper constant b_h for flutter instability diminishes rapidly, and consequently the flutter velocity increases according to (27). The frequency remains very close to $k_{r\alpha}$ in all the unstable region.

The results plotted in Fig. 7 are for $a = -1/2$, which roughly corresponds to the pivot point location with the largest growth rate for the rigid foil with constant mass ratio. Similar behaviour is found for other values of a close to the quarter-chord point, for which the rigid foil is unstable below a critical value of b_h, as discussed in Section 4.2. However, as S decreases some new flutter instability modes may arise for certain ranges of the pivot point location. To appreciate this effect, Fig. 8(a) shows contours of the growth rate $(-\sigma)$ in the pivot point — stiffness plane for one of the most unstable cases described in Section 4 for a rigid foil with constant mass ratio $R = 2$: $k_h = 0.75$, $b_h = 0.5$ and $k_\alpha = 0.5$. As discussed

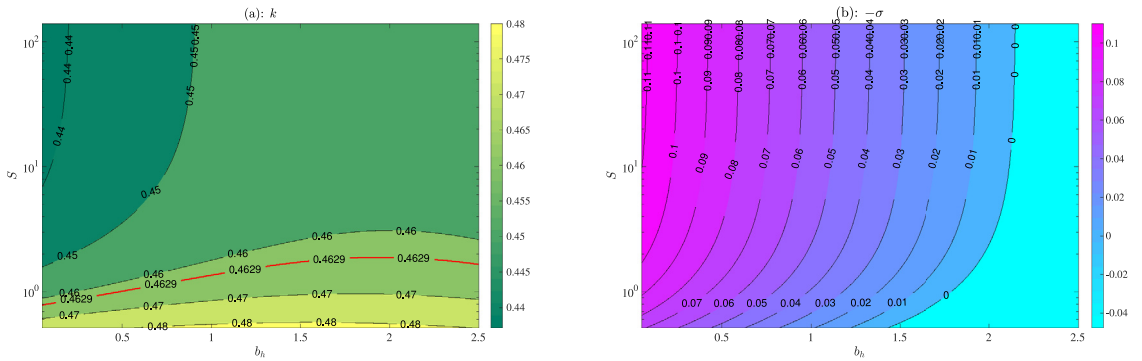

Fig. 7. Contours of frequency k (a) and growth rate $-\sigma$ (b) in the $b_h - S$ plane for a constant mass ratio foil with $b_\alpha = 0$, $m = 8$, $k_h = 0.5$, $k_\alpha = 0.5$, $a = -1/2$. The red thick line in (a) is $k_{r\alpha}$. (For interpretation of the references to colour in this figure legend, the reader is referred to the web version of this article.)

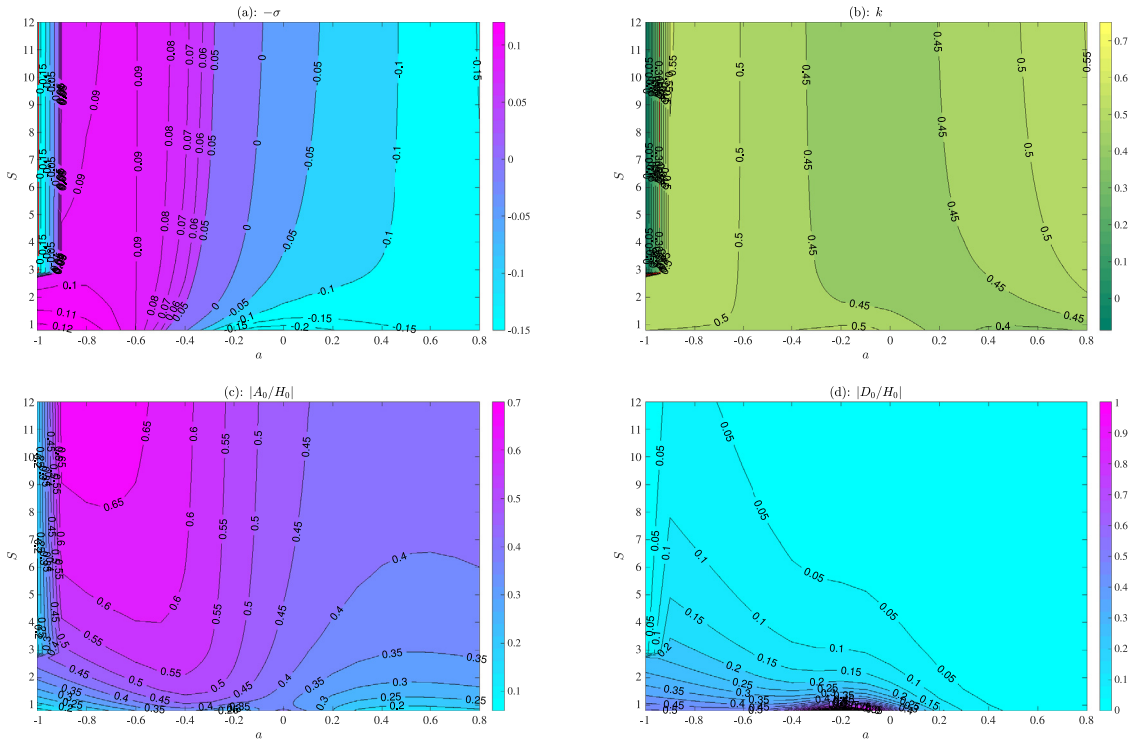

Fig. 8. Contours in the pivot − stiffness plane of the growth rate $-\sigma$ (a), frequency k (b), relative pitching amplitude $|A_0/H_0|$ (c) and relative flexural deflection amplitude $|D_0/H_0|$ (d) for a uniform foil with $m = 8$ ($R = 2$), $b_\alpha = 0$, $k_h = 0.75$, $b_h = 0.5$ and $k_\alpha = 0.5$.

in Section 4.2, for sufficiently large stiffness S the flutter stability occurs for pivots around the quarter-chord, in a band between slightly downstream of the leading edge and slightly upstream of the mid-chord. Particularly, $-0.9 \lesssim a \lesssim -0.1$ for the case plotted in Fig. 7. As S decreases, the extent of this band decreases slowly because its downstream limit moves towards the leading edge. For each value of a the corresponding frequency remains practically constant [see Fig. 8(b)] and approximately equal to the pitching resonant value, which for a foil with uniform mass is $k_{r\alpha} = \{2k_\alpha/[m(a^2 + 1/3)]\}^{1/2}$. As shown in Fig. 8(c) and (d), this "rigid" unstable mode is basically associated to the coupled pitch–plunge motion of the foil, with practically no passive flexural deflection: the largest values of the growth rate are roughly associated to the largest values of the relative pitch amplitude $|A_0/H_0|$, with negligible flexural deflection amplitude $|D_0/H_0|$.

As S approaches unity, different instability modes arise which are different from the "rigid" mode just described because they are mainly associated to the flexural deflection amplitude $|D_0|$. These "soft" unstable modes continue as S decreases below unity, becoming the most unstable ones. They are similar to the different "flag" modes obtained by Alben (2008) for a clamped foil at the leading edge when $S \lesssim 1$. But, as just discussed in Section 5.1, they are beyond the validity

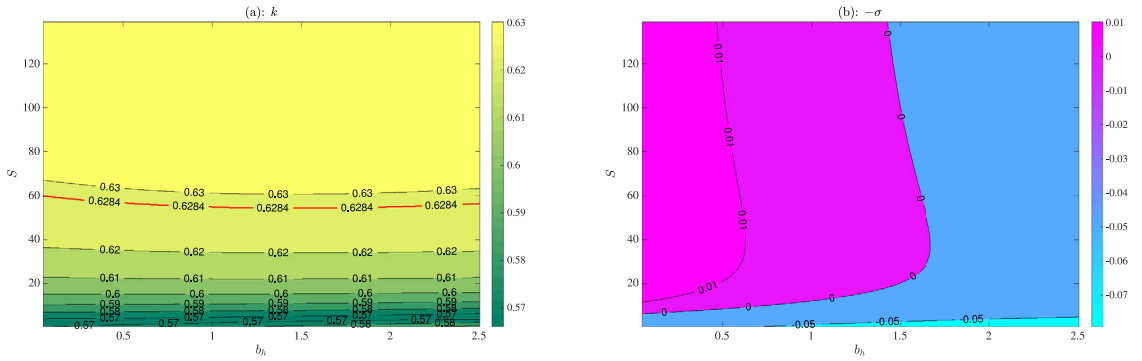

Fig. 9. Contours of frequency k (a) and growth rate $-\sigma$ (b) in the $b_h - S$ plane for the case with $k_h = 2.5$ in Fig. 2. The red line in (a) is $k_{r\alpha}$. (For interpretation of the references to colour in this figure legend, the reader is referred to the web version of this article.)

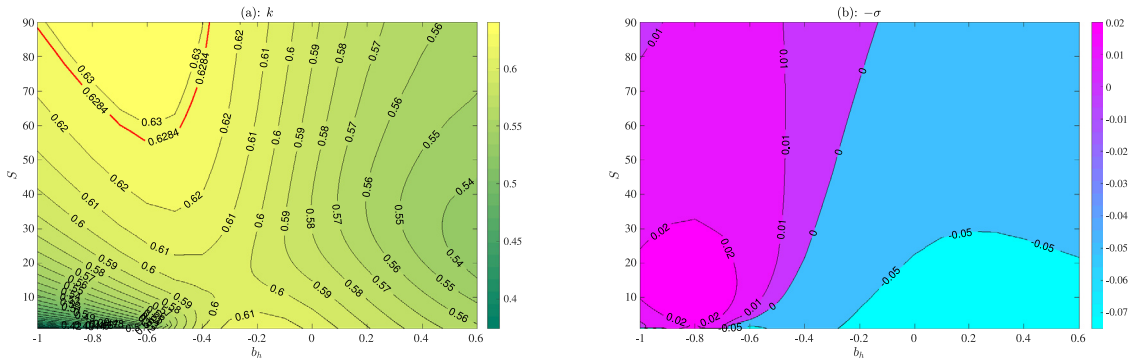

Fig. 10. Contours in the pivot − stiffness plane of the frequency k (a) and growth rate $-\sigma$ (b) for $b_\alpha = 0$, $m = 8$, $I_a = 32$, $k_\alpha = 6.32$, $b_h = 0.5$, $k_h = 2.5$ and $x_0 = a + 0.4$.

range of the present approximation. A similar behaviour is found for other values of the mass ratio R provided that it is large enough for the existence of rigid-foil unstable modes ($R \gtrsim 1$).

As a final example we consider the effect of finite stiffness on the onset of instability for the case plotted in Fig. 2, which is one of the foil configurations considered numerically by Boudreau et al. (2020). In particular, Fig. 9 shows the results for the value $k_h = 2.5$ in Fig. 2 as the stiffness S decreases. Remember that this case is for a foil pivoting at the quarter-chord ($a = -1/2$). Contrary to the foil with uniform mass ratio plotted in Fig. 7, now the instability region first increases slowly as S decreases from infinity, and then decreases rapidly until it disappears for S below approximately six. The most unstable case (i.e., with the largest critical value of b_h, or the lowest flutter velocity) is found now for $S \approx 40$, well within the validity range of the present model. The corresponding frequency decreases slightly with S, but always close to the resonant frequency $k_{r\alpha}$.

As S decreases for other pivot axis locations, the instability pattern may be quite different. This can be observed in Fig. 10, where the growth rate and the frequency is plotted in the $a - S$ plane for same spring stiffness $k_h = 2.5$ and $b_h = 0.5$, well within the unstable regions plotted in Figs. 2 and 9. It must be noted that now one has to modify the centre of mass x_0 as the pivot point location a is varied, because in this configuration considered by Boudreau et al. (2020) the static moment $S^* = m(x_0 - a)/8$ (see Table 1) is constant and equal to 0.4. Thus, $x_0 = 0.4 + a$, and we plot the interval $-1 < a < 0.6$. It is observed that, as S decreases, the foil becomes more unstable when the pivot point displaces towards the leading edge, with maximum growth rate for $a \approx -0.85$, when $S \approx 15$. The rigid-foil instability of the quarter-chord point disappears as S approaches unity, as already observed in Fig. 9.

6. Concluding remarks

A simple analytical tool for determining the onset of flutter instability of an elastically supported flexible, two-dimensional foil in an incompressible and inviscid flow has been developed. The formulation may be used to derive a first estimation of the operating and near optimal conditions of fully-passive flapping-foil turbines, covering without much effort the complete set of nondimensional parameters that may affect to the performance of these energy harvesting devices: mass, centre of mass, characteristics of the translational and torsional springs and dampers, pivot axis location, stiffness, moment of inertia and all the other dimensionless parameters characterizing the coupling between the

chordwise flexural deflection with the pitch and plunge motions, which are determined from the chordwise mass ratio distribution of the foil. The analysis also provides the corresponding leading frequency of the oscillations originated from the flutter instability, valid for stiffness ratios larger than about unity. Thus, given the velocity of the fluid current and other structural requirements of the elastically supported foil one may select appropriate values of the remaining parameters to start searching for the optimal configuration for energy harvesting. This last task that has to be done either numerically or experimentally, because the subsequent non-linear evolution of the system after the onset of instability, and therefore the power output and the efficiency, cannot be obtained from the present formulation for a fully-passive system. Other non-linear phenomena such as stall flutter, hysteresis, three-dimensional effects, subcritical transitions, decoupling between the different components of the oscillations, etc., which may also affect the energy harvesting performance, are obviously not considered here either. But the coupling of the foil's flexural deflection with the pitch and plunge motions of a foil elastically mounted to translational and torsional springs and dampers at arbitrary pivot axis locations has not been considered before, to our knowledge, in previous studies on the onset of flutter instability.

CRediT authorship contribution statement

R. Fernandez-Feria: Conceptualization, Methodology, Data curation, Formal analysis, Funding acquisition, Investigation, Project administration, Software, Supervision, Validation, Visualization, Writing – original draft, Writing – review & editing.

Declaration of competing interest

The authors declare that they have no known competing financial interests or personal relationships that could have appeared to influence the work reported in this paper.

Acknowledgement

This research has been financed by the Ministerio de Ciencia e Innovación of Spain (PID2019-104938RB-I00). Funding for open access charge: Universidad de Málaga / CBUA.

Appendix A. Coefficients in Eqs. (5)–(7)

A.1. For constant mass ratio R

When the nondimensional mass ratio R is constant, the coefficients (10)–(15) are:

$$m = 4R\,, \quad m(x_0 - a) = -4aR\,, \qquad x_0 = 0\,, \tag{A.1}$$

$$I_a = 4R\left(\frac{1}{3} + a^2\right)\,, \tag{A.2}$$

$$J_a = 2R\left[a^2 - \frac{2}{3}a - \frac{1}{3} + \frac{16}{15(1-a)^2}\right]\,, \tag{A.3}$$

$$I_d = -4Ra\left(1 + a^2\right)\,, \tag{A.4}$$

$$J_d = 2R\frac{-12 - 93a + 60a^2 - 110a^3 + 120a^4 - 45a^5}{45(1-a)^2}\,, \tag{A.5}$$

$$K_d = 2R\frac{141 + 168a + 1281a^2 - 1120a^3 + 1015a^4 - 840a^5 + 315a^6}{315(1-a)^2}\,. \tag{A.6}$$

A.2. For given m, x_0 and I_a

One can select the foil's density distribution $\rho_s(x)$, and hence $R(x)$, to obtain particular values of the coefficients. It is physically relevant, for instance, to fix m, x_0 and I_a independently for a given pivot a. This can be achieved in a simple way by selecting a uniform distribution with two localized masses; i.e.,

$$R(x) = R_0 + B\delta(x-b) + D\delta(x-d)\,, \tag{A.7}$$

where δ is Dirac's delta function and R_0, B, D, b and d are unknown constants, with $-1 < b, d < 1$. From the definitions (10)–(11), one gets a system of three linear equations for R_0, B and D,

$$m = 4R_0 + 2B + 2D\,, \quad x_0 = 2bB + 2dD\,, \quad I_a = 4R_0\left(a^2 + \frac{1}{3}\right) + 2(b-a)^2 B + 2(d-a)^2 D\,, \tag{A.8}$$

which can be solved for given m, x_0, I_a and a, and selecting b and d that yield positive values of m, x_0 and I_a. Then, the remaining coefficients J_a, I_d, J_d and K_d are easily obtained from their definitions because the integrals involving delta functions are straightforward, and the remaining terms containing R_0 are given by (A.3)–(A.6) replacing R by R_0.

Appendix B. Lift, moment and flexural coefficients

The coefficients corresponding to the quartic foil's deflection (2) are derived in Fernandez-Feria and Alaminos-Quesada (2021a,b) for a harmonic motion with reduced frequency k, i.e., when $\gamma = k$. Thus, k is replaced in the following expressions by the complex quantity $\gamma = k + i\sigma$:

$$C_L(t) = \pi\left[-\ddot{h} - a\ddot{\alpha} + \dot{\alpha} + A_{l2}(a)\ddot{d} + A_{l1}(a)\dot{d}\right] + \mathcal{C}(\gamma)\Gamma_0(t)\,, \tag{B.1}$$

$$C_M(t) = \frac{\pi}{2}\left[a\ddot{h} + \left(a^2 + \frac{1}{8}\right)\ddot{\alpha} + \left(\frac{1}{2} - a\right)\dot{\alpha} + A_{m2}(a)\ddot{d} + A_{m1}(a)\dot{d} + A_{m0}(a)d\right] - \frac{1}{2}\left(\frac{1}{2} + a\right)\mathcal{C}(\gamma)\Gamma_0(t)\,, \tag{B.2}$$

$$C_F(t) = \pi\left[-\left(a^2 + \frac{1}{4}\right)\ddot{h} - a\left(a^2 + \frac{1}{2}\right)\ddot{\alpha} + a(a-1)\dot{\alpha} + A_{f2}(a)\ddot{d} + A_{f1}(a)\dot{d} + A_{f0}(a)d\right] + \left(\frac{1}{2} + a + a^2\right)\mathcal{C}(\gamma)\Gamma_0(t)\,, \tag{B.3}$$

where

$$\Gamma_0(t) = -2\pi\left[\dot{h} + \left(a - \frac{1}{2}\right)\dot{\alpha} - \alpha + A_{g1}(a)\dot{d} + A_{g0}(a)d\right] \tag{B.4}$$

is the quasi-steady circulation, being

$$\mathcal{C}(\gamma) = \frac{H_1^{(2)}(\gamma)}{iH_0^{(2)}(\gamma) + H_1^{(2)}(\gamma)} = \mathcal{F}(\gamma) + i\mathcal{G}(\gamma) \tag{B.5}$$

Theodorsen's function (Theodorsen, 1935), and $H_n^{(2)}(z) = J_n(z) - iY_n(z)$, $n = 0, 1$, Hankel's function of the second kind and order n, related to the Bessel functions of the first and second kind $J_n(z)$ and $Y_n(z)$ (Olver et al., 2010), and where the following functions of the pivot point location a have been defined:

$$A_{l2} = -\frac{13 + 48a^2 - 64a^3 + 24a^4}{48(1-a)^2}\,, \quad A_{l1} = \frac{3 + 12a - 12a^2 + 4a^3}{6(1-a)^2}\,, \tag{B.6}$$

$$A_{m2} = \frac{2 + 25a - 12a^2 + 52a^3 - 64a^4 + 24a^5}{48(1-a)^2}\,, \quad A_{m1} = \frac{-9 + 12a - 72a^2 + 56a^3 - 16a^4}{24(1-a)^2}\,, \tag{B.7}$$

$$A_{m0} = -\frac{3}{4(1-a)^2}\,, \quad A_{f2} = -\frac{35 + 32a + 392a^2 - 320a^3 + 496a^4 - 512a^5 + 192a^6}{384(1-a)^2}\,, \tag{B.8}$$

$$A_{f1} = \frac{1 + 8a - 18a^2 + 48a^3 - 32a^4 + 8a^5}{12(1-a)^2}\,, \quad A_{f0} = \frac{7 + 18a}{12(1-a)^2}\,, \tag{B.9}$$

$$A_{g1} = \frac{15 - 48a + 96a^2 - 80a^3 + 24a^4}{48(1-a)^2}\,, \quad A_{g0} = \frac{3 - 24a + 24a^2 - 8a^3}{12(1-a)^2}\,. \tag{B.10}$$

Appendix C. Coefficients in Eq. (18)

These coefficients are

$$A_{11} = -m\gamma^2 + k_h + b_h i\gamma + A_{11}^F\,, \tag{C.1}$$

$$A_{12} = -m\gamma^2(a - x_0) + A_{12}^F\,, \tag{C.2}$$

$$A_{13} = -J_a\gamma^2 + A_{13}^F\,, \quad A_{21} = m\gamma^2(a - x_0) + A_{21}^F\,, \tag{C.3}$$

$$A_{22} = I_a\gamma^2 - 2k_\alpha - 2b_\alpha i\gamma + A_{22}^F\,, \tag{C.4}$$

$$A_{23} = -J_d\gamma^2 + A_{23}^F\,, \quad A_{31} = -I_a\gamma^2 + A_{31}^F\,, \quad A_{32} = I_d\gamma^2 + A_{32}^F\,, \tag{C.5}$$

$$A_{33} = -K_d\gamma^2 + \frac{16}{3}\frac{a^2 + \dfrac{1}{3}}{(1-a)^2}\,S + A_{33}^F\,, \tag{C.6}$$

where the superscript F refers to the contributions to these coefficients from the fluid–structure interaction (i.e., from C_L, C_M and C_F). Using the expressions of C_L, C_M and C_F in Appendix B, these contributions can be written as

$$A_{11}^F = \pi\gamma[-\gamma + 2i\mathcal{C}(\gamma)]\,, \tag{C.7}$$

$$A_{12}^F = -\pi\left\{a\gamma^2 + i\gamma + 2\mathcal{C}(\gamma)\left[1 - i\gamma\left(a - \frac{1}{2}\right)\right]\right\}\,, \tag{C.8}$$

$$A_{13}^F = \pi\left[A_{l2}\gamma^2 - A_{l1}i\gamma + 2\mathcal{C}(\gamma)(A_{g1}i\gamma + A_{g0})\right]\,, \tag{C.9}$$

$$A_{21}^F = \pi\left[a\gamma^2 - \mathcal{C}(\gamma)\,(2a+1)\,i\gamma\right]\,, \tag{C.10}$$

$$A_{22}^F = -\pi\left\{-\left(a^2 + \frac{1}{8}\right)\gamma^2 + \left(\frac{1}{2} - a\right)i\gamma + \mathcal{C}(\gamma)(2a+1)\left[i\gamma\left(a - \frac{1}{2}\right) - 1\right]\right\}\,, \tag{C.11}$$

$$A_{23}^F = -\pi\left[-A_{m2}\gamma^2 + A_{m1}i\gamma + A_{m0} + \mathcal{C}(\gamma)(2a+1)\left(A_{g1}i\gamma + A_{g0}\right)\right]\,, \tag{C.12}$$

$$A_{31}^F = \pi\left[-\left(a^2 + \frac{1}{4}\right)\gamma^2 + \mathcal{C}(\gamma)(2a^2 + 2a + 1)i\gamma\right]\,, \tag{C.13}$$

$$A_{32}^F = -\pi\left\{\left(a^2 + \frac{1}{2}\right)a\gamma^2 + a(a-1)i\gamma + \mathcal{C}(\gamma)(2a^2 + 2a + 1)\left[1 - i\gamma\left(a - \frac{1}{2}\right)\right]\right\}\,, \tag{C.14}$$

$$A_{33}^F = \pi\left[A_{f2}\gamma^2 - A_{f1}i\gamma - A_{f0} + \mathcal{C}(\gamma)(2a^2 + 2a + 1)\left(A_{g1}i\gamma + A_{g0}\right)\right]\,. \tag{C.15}$$

References

Abiru, H., Yoshitake, A., 2011. Study on a flapping wing hydroelectric power generation system. J. Environ. Eng. 6 (178).
Alaminos-Quesada, J., Fernandez-Feria, R., 2020. Propulsion of a foil undergoing a flapping undulatory motion from the impulse theory in the linear potential limit. J. Fluid Mech. 883 (A19), 1–24.
Alben, S., 2008. The flapping-flag instability as a nonlinear eigenvalue problem. Phys. Fluids 20, 104106.
Amandolese, X., Michelin, S., Choquel, M., 2013. Low speed flutter and limit cycle oscillations of a two-degree-of-freedom flat plate in a wind tunnel. J. Fluids Struct. 43, 244–255.
Bisplinghoff, R.L., Ashley, H., 1975. Principles of Aeroelasticity. Dover, New York.

Boragno, C., Festa, R., Mazzino, A., 2012. Elastically bounded flapping wing for energy harvesting. Appl. Phys. Lett. 100, 253906.
Boudreau, M., Dumas, G., Rahimpour, M., Oshkai, P., 2018. Experimental investigation of the energy extraction by a fully-passive flapping-foil hydrokinetic turbine prototype. J. Fluids Struct. 82, 446–472.
Boudreau, M., Gunther, K., Dumas, G., 2019a. Free-pitching flapping-foil turbines with imposed sinusoidal heave. J. Fluids Struct. 90, 110–138.
Boudreau, M., Gunther, K., Dumas, G., 2019b. Investigation of the energy-extraction regime of a novel semi-passive flapping-foil turbine concept with a prescribed heave motion and a passive pitch motion. J. Fluids Struct. 84, 368–390.
Boudreau, M., Picard-Deland, M., Dumas, G., 2020. A parametric study and optimization of the fully-passive flapping-foil turbine at high Reynolds number. Renew. Energy 146, 1958–1975.
Dowell, E. H. e., 2015. A Modern Course in Aeroelasticity, fifth ed. Springer, New York.
Duarte, L., Dellinger, N., Dellinger, G., Ghenaim, A., Terfous, A., 2019. Experimental investigation of the dynamic behaviour of a fully passive flapping foil hydrokinetic turbine. J. Fluids Struct. 88, 1–12.
Fernandez-Feria, R., 2016. Linearized propulsion theory of flapping airfoils revisited. Phys. Rev. Fluids 1, 084502.
Fernandez-Feria, R., Alaminos-Quesada, J., 2021a. Analytical results for the propulsion performance of a flexible foil with prescribed pitching and heaving motions and passive small deflection. J. Fluid Mech. 910 (A43).
Fernandez-Feria, R., Alaminos-Quesada, J., 2021b. Propulsion and energy harvesting performances of a flexible thin airfoil undergoing forced heaving motion with passive pitching and deformation of small amplitude. J. Fluids Struct. 102, 103255.
Floryan, D., Rowley, C.W., 2018. Clarifying the relationship between efficiency and resonance for flexible inertial swimmers. J. Fluid Mech. 853, 271–300.
Fung, Y.C., 1969. An Introduction to the Theory of Aeroelasticity. Dover, New York.
Guo, C.Q., Païdoussis, M.P., 2000. Stability of rectangular plates with free side-edges in two-dimensional inviscid channel flow. J. Appl. Mech. 67, 171–176.
Kinsey, T., Dumas, G., 2008. Parametric study of an oscillating airfoil in a power-extraction regime. AIAA J. 46 (6), 1318–1330.
Liu, W., Xiao, Q., Cheng, F., 2013. A bio-inspired study on tidal energy extraction with flexible flapping wings. Bioinspir. Biomim. 8, 036011.
Ma, P., Liu, G., Wang, Y., Zhang, Y., Xie, Y., 2021. Numerical study on the hydrodynamic performance of a semi-passive oscillating hydrofoil. Ocean Eng. 223, 108649.
Olver, F.W.J., Lozier, D.W., Boisvert, R.F., Clark, C.W. (Eds.), 2010. NIST Handbook of Mathematical Functions. Cambridge University Press, Cambridge (UK).
Peng, Z., Zhu, Q., 2009. Energy harvesting through flow-induced oscillations on a foil. Phys. Fluids 21, 123602.
Pigolotti, L., Mannini, C., Bartoli, G., Thiele, K., 2017. Critical and post-critical behaviour of two-degree-of-freedom flutter-based generators. J. Sound Vib. 404, 116–140.
Poirel, D., Mendes, F., 2014. Experimental small-amplitude self-sustained pitch-heave oscillations at transitional Reynolds numbers. AIAA J. 52, 1581–1590.
Sears, W.R., 1941. Some aspects of non-stationary airfoil theory and its practical application. J. Aeronaut. Sci. 8, 104–108.
Shimizu, E., Isogai, K., Obayashi, S., 2008. Multiobjective design study of a flapping wing power generator. J. Fluids Eng. 130, 021104.
Su, Y., Breuer, K., 2019. Resonant response and optimal energy harvesting of an elastically mounted pitching and heaving hydrofoil. Phys. Rev. Fluids 4, 064701.
Tang, L., Païdoussis, M.P., 2007. On the instability and the post-critical behaviour of two-dimensional cantilevered flexible plates in axial flow. J. Sound Vib. 305, 97–115.
Tang, L., Païdoussis, M.P., Jiang, J., 2009. Cantilevered flexible plates in axial flow: Energy transfer and the concept of flutter-mill. J. Sound Vib. 326, 263–276.
Theodorsen, T., 1935. General Theory of Aerodynamic Instability and the Mechanism of Flutter. Tech. Rep. TR 496, NACA.
Veilleux, J.C., Dumas, G., 2017. Numerical optimization of a fully-passive flapping-airfoil turbine. J. Fluids Struct. 70, 102–130.
von Kármán, T., Sears, W.R., 1938. Airfoil theory for non-uniform motion. J. Aeronaut. Sci. 5, 379–390.
Wang, Z., Du, L., Zhao, J., Sun, X., 2017. Structural response and energy extraction of a fully passive flapping foil. J. Fluids Struct. 72, 96–113.
Xiao, Q., Zhu, Q., 2014. A review on flow energy harvesting based on flapping foils. J. Fluids Struct. 46, 174–191.
Young, J., Lai, J.C.S., Platzer, M.F., 2014. A review of progress and challenges in flapping foil power generation. Prog. Aerosp. Sci. 67, 2–28.
Zhu, Q., 2012. Energy harvesting by a purely passive flapping foil from shear flows. J. Fluids Struct. 34, 157–169.
Zhu, Q., Haase, M., Wu, C.H., 2009. Modeling the capacity of a novel flow-energy harvester. Appl. Math. Model. 130, 2207–2217.
Zhu, Q., Peng, Z., 2009. Mode coupling and flow energy harvesting by a flapping foil. Phys. Fluids 21, 033601.
Zhu, Y., Su, Y., Breuer, K., 2020. Nonlinear flow-induced instability of an elastically mounted pitching wing. J. Fluid Mech. 899 (A35).